Journal Pre-proofs

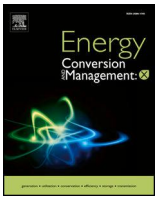

Prediction of three-dimensional temperature and current density field distribution in solid oxide electrolysis cells by modified transformer

Fangzhou Wang, Fan Yang, Lily Wu, Hao Wang, Jun Cao

PII: S2590-1745(25)00319-8
DOI: https://doi.org/10.1016/j.ecmx.2025.101187
Reference: ECMX 101187

To appear in: *Energy Conversion and Management: X*

Received Date: 12 June 2025
Revised Date: 22 July 2025
Accepted Date: 5 August 2025

Please cite this article as: F. Wang, F. Yang, L. Wu, H. Wang, J. Cao, Prediction of three-dimensional temperature and current density field distribution in solid oxide electrolysis cells by modified transformer, *Energy Conversion and Management: X* (2025), doi: https://doi.org/10.1016/j.ecmx.2025.101187

Prediction of Three-dimensional Temperature and Current Density Field Distribution in Solid Oxide Electrolysis Cells by Modified Transformer

Fangzhou Wang [1] , Fan Yang [2]* , Lily Wu [1] , Hao Wang [1] , Jun Cao [1]*

(1.East China University of Science and Technology, 130 Meilong Road, Xuhui, Shanghai, China 200237;

2.Chengdu University of Information Technology, No.24 Block 1, Xuefu Road, Chengdu, China 610225)

Abstract:

The temperature distribution spatial contour of solid oxide electrolysis cells (SOECs) is a critical indicator for evaluating device performance, energy consumption, and maintenance safety. Conventional computational fluid dynamics (CFD) simulations, while accurate, suffer from excessive computational time and poor timeliness, making them unsuitable for real-time field monitoring. To address this, this paper proposes an improved Transformer neural network model driven by CFD data for real-time prediction of SOEC internal temperature field spatial contours. The model integrates a hybrid architecture of CNN and Transformer, where a multi-coupled CNN extracts operational parameter features, and a positional encoding Transformer reconstructs the spatial distribution of physical fields. Experimental results show that the model completes temperature field reconstruction within seconds, reducing computational resource consumption by over 90% compared to traditional CFD methods. In terms of accuracy, the mean absolute error (MAE) of temperature field prediction is controlled below 2 K, and the

current density field prediction accuracy exceeds 95%. This approach breaks through the timeliness bottleneck of conventional simulations, provides an efficient and reliable technical support for intelligent operation and maintenance of SOEC digital twins and demonstrates significant engineering value for enhancing the operational stability and intelligent management of SOEC systems.

Key words: SOEC; CFD; Transformer; Physical field distribution prediction;

Corresponding author: Dr. Jun Cao ; Dr. Fan Yang

Tel: 86-21-64253810 Fax: 86-21-642533810; Tel: 86-18113090521

Email: caojun@ecust.edu.cn ; Email: yang.fan@live.com

*：The authors contributed equally to this work as co-corresponding authors.

1. Introduction

With the escalating global energy crisis, hydrogen energy, as a quintessential clean energy carrier, has garnered increasing attention[1-2]. Among mainstream hydrogen production technologies, biomass-based hydrogen production suffers from high costs, while fossil fuel reforming exhibits limited environmental benefits. In contrast, water electrolysis stands out for its capability to integrate renewable energy sources (e.g., hydropower and wind power), offering distinct advantages of low-carbon emission and broad industrial prospects[3-5]. Common electrolysis technologies include alkaline electrolyzers (ALK), proton exchange

membrane electrolyzers (PEM), and solid oxide electrolyzers (SOEC). Unlike ALK and PEM, which operate below 200 °C, SOECs function at 600-1000 °C, enabling superior energy efficiency (80%-100%) and accelerated reaction kinetics due to elevated temperatures[6-9]. This makes SOEC a promising technology for large-scale industrial hydrogen production.

However, the high operating temperature of SOECs necessitates real-time monitoring and regulation of internal thermal conditions to ensure optimal performance, energy efficiency, and safety, particularly to prevent localized overheating. Conventional methods, such as manual thermocouple measurements or discrete sensor placement, only provide partial hotspot data, failing to capture the full temperature field distribution. Although computational fluid dynamics (CFD) simulations can model the entire temperature field, they suffer from severe limitations: the complex internal structure of SOECs demands hours of computation on standard hardware, rendering them inadequate for real-time applications.

Additionally, the internal current density distribution is a critical metric for residual life assessment and operational optimization of SOECs. Given that practical SOEC systems typically consist of dozens of stacked single-cell plates, in-situ monitoring of electrolyte layers is infeasible, while CFD simulation remains computationally intractable.

Recent advances in CFD-driven neural network models offer a viable solution. By leveraging trained neural networks, these models can reconstruct 3D temperature and current density fields by interpolating key nodal data. The predicted fields are then visualized in real-time as spatial contour maps via point cloud technology on a Unity3D-based digital twin platform, enabling intelligent operation and maintenance.

Current research on neural network-based temperature field reconstruction has seen notable progress:

Zheng et al.[10] proposed a HISM-RCM hybrid framework combining temporal convolution and a heat input sensing method, achieving 99.76% accuracy in mechanical machining temperature monitoring.

Chen et al.[11] employed physics-informed neural networks (PINN) with transfer learning for launch vehicle thermal protection systems, achieving single-digit mean absolute error in temperature prediction.

Hu et al.[12] developed a Swin Transformer framework for 3D forging mold temperature fields, achieving 0.98s prediction time and 0.8658°C average error.

However, these models—including autoencoders and convolutional networks—exhibit limited performance when applied to the complex, non-linear SOEC physical fields. This study presents a modified Transformer model tailored for SOECs, as detailed in subsequent sections, the model uniquely fuses a multi-coupled CNN for feature extraction and positional encoding for spatial modeling—a design that reduces computational resources by over 95% compared to traditional CFD simulations and reduced MAE by 98% compared with traditional Gaussian interpolation.

Notably, this marks the first attempt to predict 3D physical field spatial contours in SOECs using a data-driven Transformer framework. The model achieves a temperature mean absolute error (MAE) within 2 K (Kelvin thermodynamic temperature) and a current density prediction accuracy exceeding 95%, enabling real-time reconstruction of temperature and current density

fields. Such performance highlights its potential for intelligent operation and maintenance of SOEC digital twins, addressing the critical need for efficient, accurate physical field monitoring in high-temperature electrolysis systems.

2. Construction Methods of Transformer Prediction Model for SOEC 3D Physical Fields

2.1 CFD Mechanism Simulation of SOEC

2.1.1 Geometric Model

The Transformer prediction model constructed in this article is driven by CFD data, therefore CFD mechanism simulation is the first fundamental work of this study. This article first constructs a model for SOEC, as shown in Figure 1, and based on this, conducts simulation calculations under different operating conditions, accumulating three-dimensional temperature and current density field simulation data for subsequent Transformer model calculations and verification.

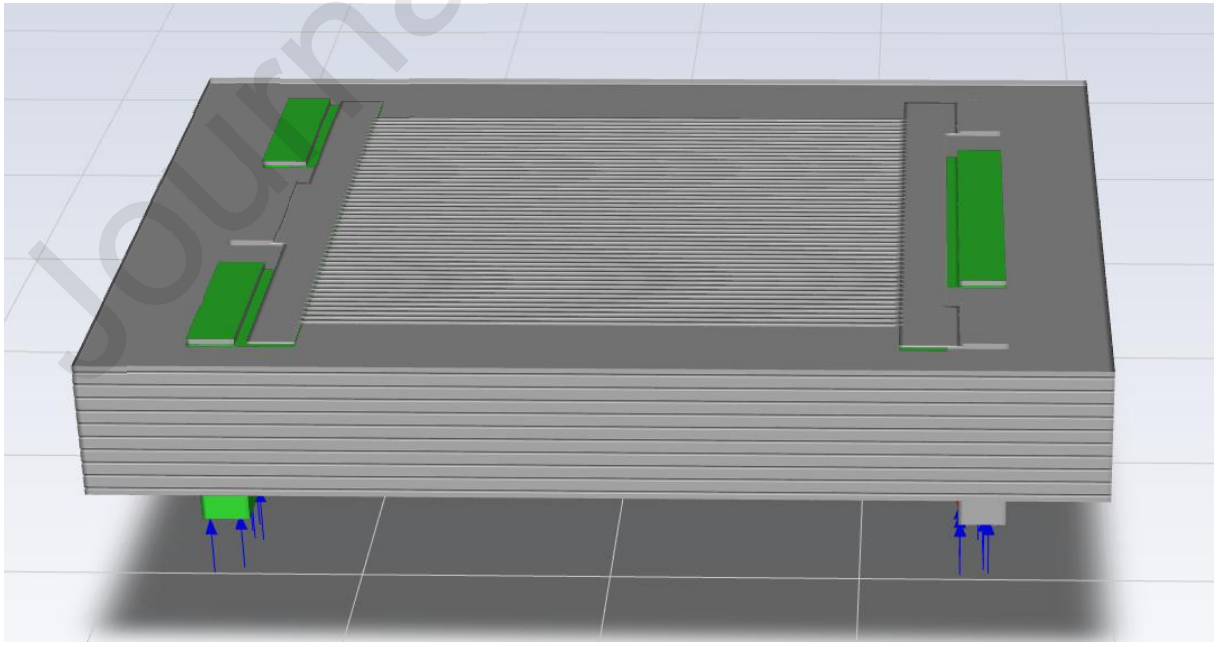

Fig.1 CFD Model of SOEC

The constructed SOEC model consists of ten layers of polar plates, each layer containing an anode connector, anode channel, anode, cathode, cathode channel, and cathode connector, as shown in Figure 2. The cathode, anode, and electrolyte have thicknesses of 10 μm, 410 μm, and 10 μm respectively, with their material compositions and key thermophysical properties specified as follows: the cathode is porous Ni-YSZ (porosity: 35%) with a thermal conductivity of 8.7 W/(m·K) and a specific heat capacity of 450 J/(kg·K); the anode is porous LSM-YSZ (porosity: 35%) characterized by a thermal conductivity of 2.1 W/(m·K) and a specific heat capacity of 500 J/(kg·K); the electrolyte is dense YSZ (porosity: <1%) with a thermal conductivity of 2.3 W/(m·K) and a specific heat capacity of 550 J/(kg·K). Each layer of polar plate is 150mm long and 120mm wide, with 30 channels separated by 29 ribs inside. Air and fuel gas (a mixture of water vapor and hydrogen) enter and exit the electrolytic cell polar plate through left and right inlet and outlet ports.

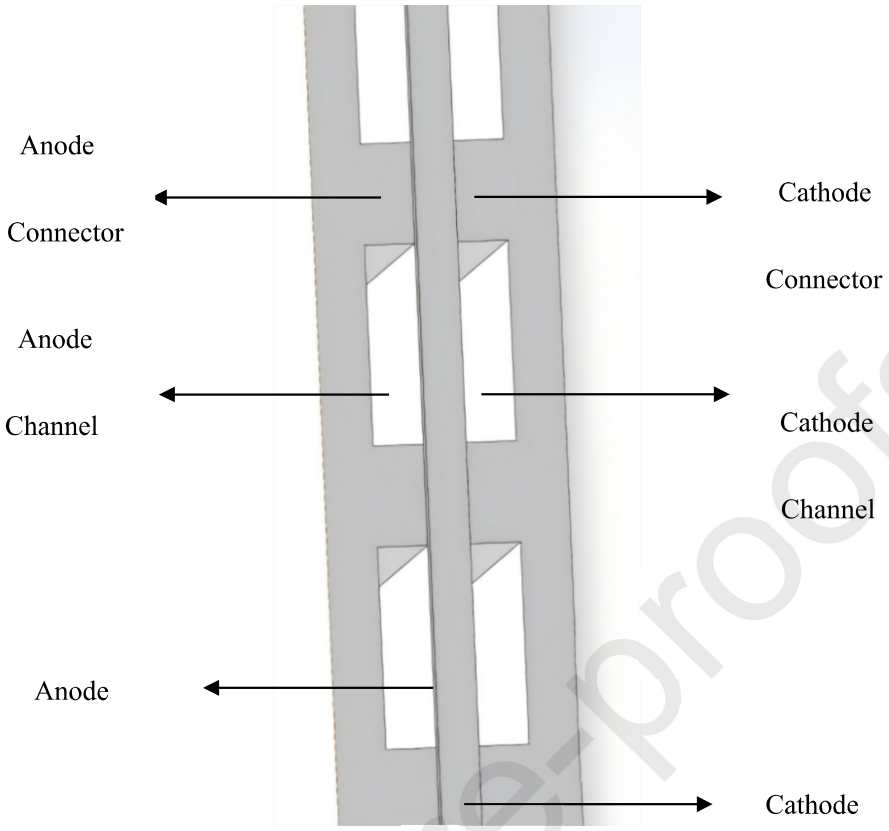

Fig.2 Diagram of Polar Plate

2.1.2 Boundary Conditions

Four main boundary condition parameters corresponding the inner temperature field distribution were set to match the actual production scenario, namely electrolysis temperature (K), electrolysis voltage (V), fuel gas water hydrogen ratio, and inlet air flow rate. The electrolysis temperature is divided into three levels: 1073 K, 1023 K, and 973 K. The electrolysis voltage is divided into three levels: 1.2V, 1.3V, and 1.4V per layer. The fuel gas water hydrogen ratio is divided into three levels: 70%, 80%, and 90%—with the inlet flow rate remaining consistent across all these levels at 0.00032 kg/s. Under these conditions, the simulated steam conversion efficiency ranged from 46.9% to 53.3%.The inlet air flow rate is also divided into three levels: 0.00065kg/s, 0.00055kg/s, and 0.00075kg/s, with a total of 81 different operating conditions.

In the thermal boundary setting of the CFD model in this article, the specific steps are as follows: the inlet gas on both sides serves as the source boundary of the thermal input, and the temperature of the inlet gas is directly set; The SOEC wall is treated with insulation to focus on the heat transfer process inside the battery; The electrode electrolyte interface is set as a thermal coupling interface without an internal heat source, and the temperature and heat flow on both sides of the interface remain continuous, ensuring that heat can be transferred between the solid and the fluid or wall through this interface.

2.1.3 Governing Equations

In the construction process of the SOEC simulation model, for the fuel side and air side inlet fluids under different boundary conditions, it is assumed that they are ideal gases, with laminar inlet flow, incompressible characteristics, and conform to the ideal gas equation, while not crossing through porous media layers. On this basis, the following control equations and electrochemical equations can be obtained:

1. According to Law of Mass Conservation:

$$\frac{\partial \rho}{\partial t} + \nabla \cdot (\rho \vec{v}) = 0 \tag{1}$$

In formula (1), ρ represents density, t represents time, ∇ represents divergence, and $\vec{v}$ represents velocity (vector). Due to the assumption that the intake fluid is an ideal gas, its density remains unchanged, and the original equation is simplified as follows:

$$\nabla \vec{v} = 0 \tag{2}$$

2. According to Law of Momentum Conservation:

$$\frac{\partial (\rho \mathrm{v})}{\partial t} + \nabla \cdot (\overrightarrow{(\rho v)} \vec{v}) = -\nabla \cdot p + \nabla \tilde{\tau} + F \tag{3}$$

In formula (3), p is the fluid pressure, $\tilde{\tau}$ is the stress tensor, and F is the volumetric force. The stress tensor $\tilde{\tau}$ can be obtained by the following formula:

$$\tilde{\tau} = \mu\left[\left(\nabla\vec{v} + \nabla\vec{v}T\right) - \frac{2}{3}\nabla\vec{v}\right] \quad (4)$$

μ is the viscosity coefficient.

3. According to Law of Energy Conservation:

$$\frac{\partial\ (\rho_g c_{pg} T)}{\partial t} + \nabla\left(\rho_g c_{pg} T\right) = \nabla\cdot\left(\lambda_g \nabla T\right) \quad (5)$$

In formula (5), ρ_g is the gas density that distinguishes it from substances in porous media, c_{pg} is the specific heat capacity of the gas, and λ_g is the thermal conductivity of the gas. The gas flow patterns in the cathode and anode channels are the same, so the governing equations are also the same.

4. When SOEC operates in production, water vapor first flows into the cathode, where it loses electrons to generate hydrogen gas and oxygen ions. Subsequently, hydrogen gas is collected and oxygen ions flow into the anode for oxidation reaction to generate oxygen gas.

Main reaction:

$$H_2O = H_2 + \frac{1}{2}O_2 \quad (6)$$

Cathode reaction:

$$H_2O + 2e^- = H_2 + O^{2-} \quad (7)$$

Anode reaction:

$$O^{2-} = 2e^- + \frac{1}{2}O_2 \quad (8)$$

2.1.4 Meshing and Model Validation

In the CFD simulation process, the mesh was generated using HyperMesh with structured

hexahedral elements, resulting in a total of 5,061,920 cells. Grid sizing was carefully optimized, with a minimum element size of 0.18 mm, maximum size of 0.79 mm, and average size of 0.46 mm. The mesh quality was rigorously controlled, featuring a minimum orthogonal quality of 0.996903 and a maximum aspect ratio of 118.195 (primarily in non-critical regions). Grid independence was systematically verified through simulations on progressively refined meshes, ensuring that key performance metrics varied by less than 3% across mesh densities.

Prior to conducting CFD simulations under different operating conditions, the SOEC mechanism model used herein was validated against experimental data from reference [13]. Following the experimental parameters, the cell structure and operating conditions were strictly replicated: cathode (Ni-YSZ), anode (LSM-YSZ), and electrolyte (YSZ) thicknesses of 15 μm, 15 μm, and 100 μm, respectively; operating conditions were set to 1023 K, 100 kPa, a fuel gas water-hydrogen ratio of 80%, with cathode and anode air molar flow rates of 36 mol/h and 30 mol/h. All geometric (electrode/electrolyte thicknesses) and operating parameters (temperature, pressure, gas flow rate, etc.) in the simulation matched those of the experiment. The verification results are shown in Figure 3.

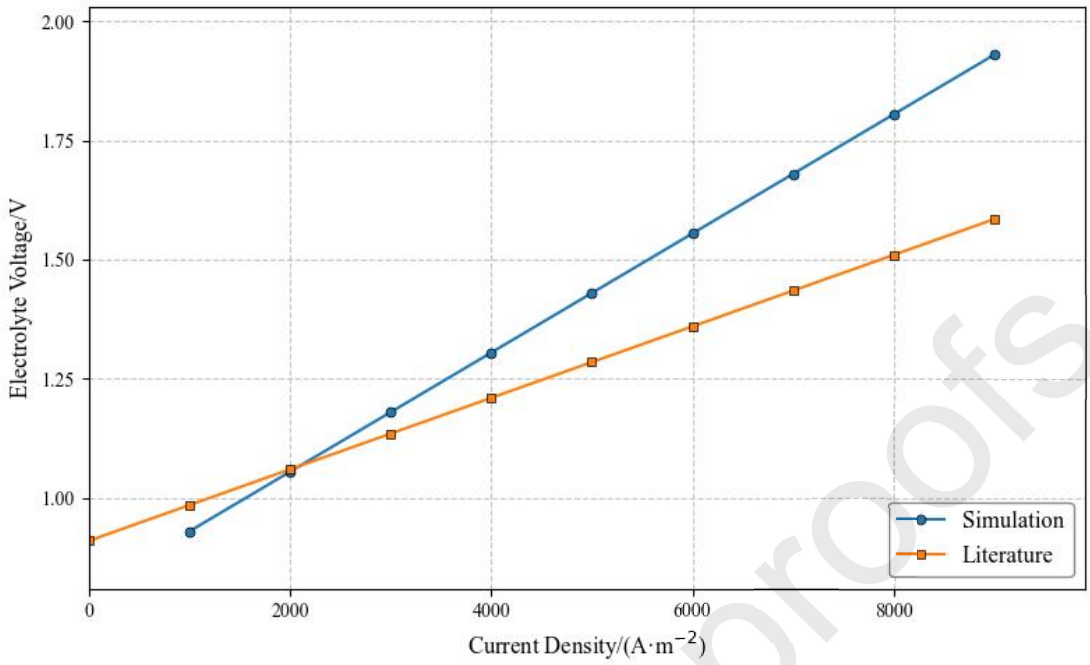

Fig.3 Comparison of CFD and Experimental Results

As is shown in Figure 3, the maximum error between the simulation results and the experimental results of the electrolysis voltage when the current density is 9000A/m^2 is 14.04%. Discrepancies between simulation and experimental data mainly stem from the following factors: simulations assume electrodes as homogeneous porous media (uniform porosity and ideal three-phase boundary distribution), whereas actual electrodes exhibit inevitable microstructural inhomogeneity (such as local porosity fluctuations and varying diffusion path tortuosity), which significantly impacts voltage at high current densities; reaction kinetic parameters in simulations rely mostly on literature empirical values, while experimental electrodes may have different catalytic activity due to preparation process variations (sintering temperature, active component content), leading to polarization voltage deviations; simulations neglect contact resistance between current collectors and electrodes as well as electrode-electrolyte interface contact loss, which are key sources of voltage deviation at low current

densities; in experiments, cathode inlet water vapor partial pressure may be lower than the set value due to pipeline condensation or humidity control errors, affecting cell voltage via the Nernst equation.

Generally speaking, the simulation results have good consistency with the experimental structure within the low current density range of non extreme operating conditions. Therefore, this article will continue to conduct mechanism simulations based on this foundation.

2.2 Construction of Modified Transformer AI-CFD Model

The AI-CFD (Artificial Intelligence-Computational Fluid Dynamics) model proposed in this study deeply integrates the encoder-decoder architecture of Transformer with the robust feature extraction capability of CNN. Innovatively, CNN is applied to the feature embedding stage of input data, enabling efficient extraction of local spatial-temporal features through multi-layer 3D convolution operations. The model leverages the weight allocation mechanism of convolutional layers to emphasize positional information, ensuring that geometric dependencies within the SOEC structure are captured. Before feeding data into the Transformer encoder, a 1D convolutional layer is strategically introduced to reduce data dimensionality while preserving critical information via a skip connection mechanism. This design effectively mitigates information loss during feature extraction, maintaining the integrity of physical field characteristics.

Preprocessed data flows through the Transformer architecture, undergoing hierarchical feature abstraction and prediction logic deduction via multi-head attention in both encoder and decoder modules—enabling the model to learn complex nonlinear relationships between

operational parameters and physical field distributions. The final output is a predicted scalar (e.g., fluid temperature, current density) for each spatial grid point, enabling full-field reconstruction. As shown in Figure 4, the architecture synergistically integrates CNN's local feature extraction with Transformer's global dependency modeling, tailored for high-precision prediction of SOEC 3D physical fields.

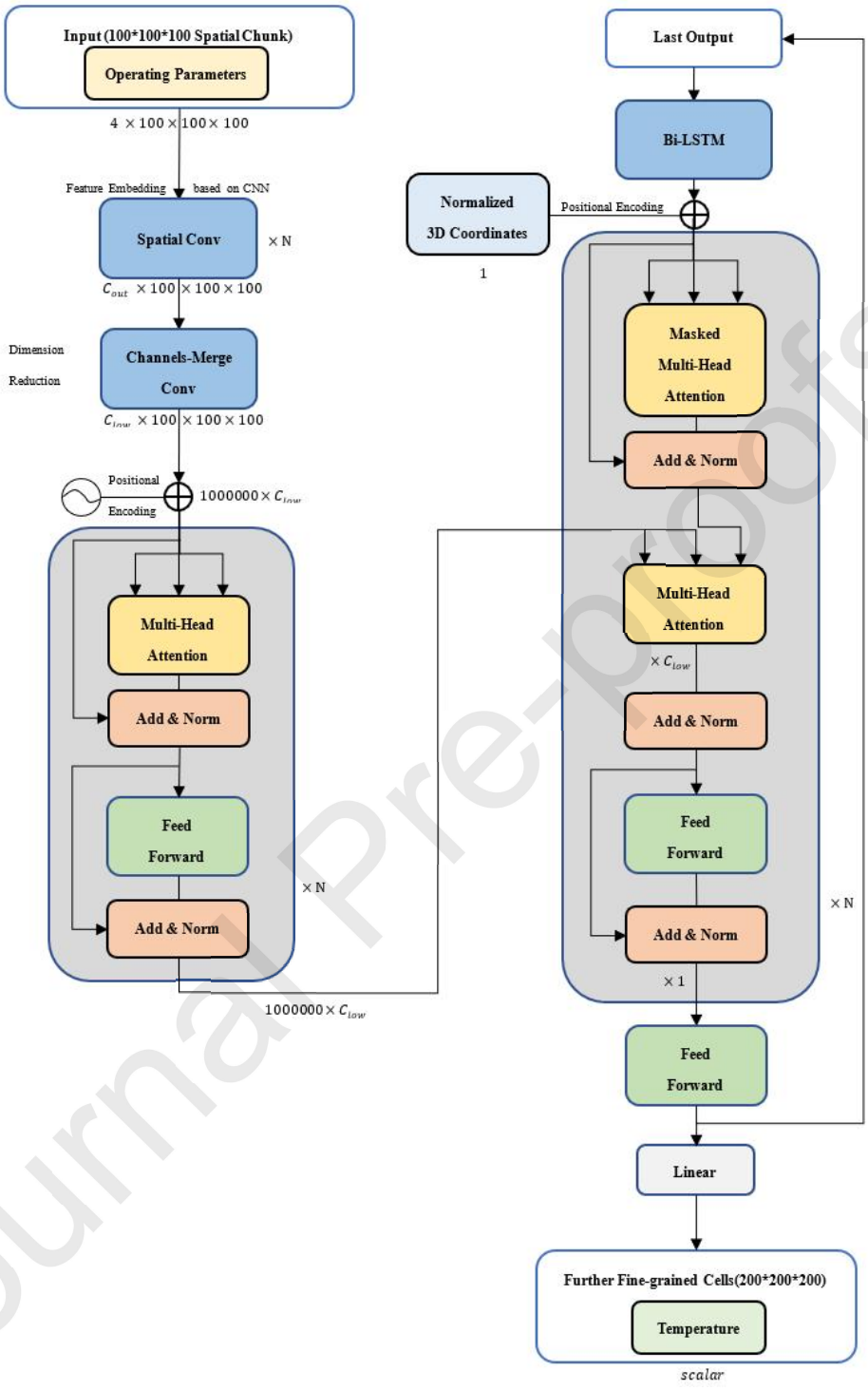

Fig.4 Overall Diagram of Modified Transformer Model

2.3 Innovation of Modified Transformer AI-CFD Model

In the AI-CFD model's network architecture, the Convolutional Block (Fig. 5) serves as a key local processing unit, meticulously composed of cascaded 3D and 1D convolutional layers.

The 3D layer first extracts spatial-channel local features from the four input operating parameter tensors via 3D convolution, effectively capturing inter-parameter coupling and spatial distributions. With the output of the 3D convolution, the subsequent 1D layer then performs sequence-wise convolution with adaptive weight allocation to encode positional information, thereby enhancing temporal dependence and spatial localization in feature representations. This two-layer design ingeniously balances local feature mining and positional encoding, forming a robust foundation for subsequent processing.

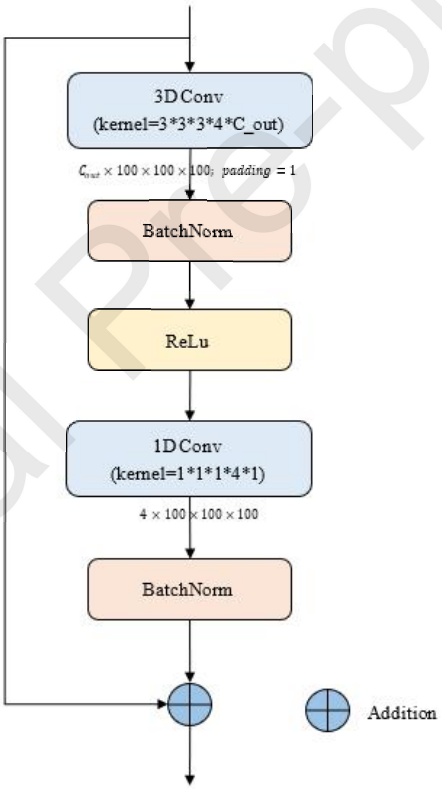

Fig.5 Diagram of Spatial Convolutional Block in CFD-AI Model

For the input of the AI-CFD model, assuming the input operating parameters (electrolysis temperature (K), electrolysis voltage (V), fuel gas water hydrogen ratio, and inlet air flow rate) are P, the distribution of each operating parameter on the three-dimensional spatial grid naturally forms a cube:

$$P_k \in \mathbb{R}^{D\times H\times W},\ \ k = 1,2,3,4 \tag{9}$$

In the context of the model, $P_k[d,h,w]$ denotes the value of the k-th operating condition parameter at the spatial coordinates (d,h,w). Here, the dimensions D (Depth), H (Height), and W (Width) are all set to 10, such that each parameter corresponds to a 10×10×10 matrix.

In three-dimensional space, the normalized coordinates （$\tilde{x},\tilde{y},\tilde{z}$） of each grid point further compose three coordinate cubic tensors, as shown in Formula (10); the normalization range is that（$\tilde{x},\tilde{y},\tilde{z}$）$\in[-1,1]$ and if $\tilde{x}$ is taken as an example (the same applies to $\tilde{y}$ and $\tilde{z}$), the relationship with the real coordinate (x,y,z) is as shown in Formula (11):

$$\tilde{x} \in \mathbb{R}^{D\times H\times W}, \tilde{y} \in \mathbb{R}^{D\times H\times W}, \tilde{z} \in \mathbb{R}^{D\times H\times W} \tag{10}$$

$$\tilde{x} = \frac{2x - (x_{max} + x_{min})}{x_{max} - x_{min}} \tag{11}$$

When inputting into the Spatial convolutional layer, 3D convolution is first applied to capture inter-parameter coupling and spatial distributions. During this process, the dimension of the input tensor X is as specified in Formula (12), while the dimension of the convolution kernel tensor K is detailed in Formula (13). The calculation formula for the output tensor of the 3D convolution, along with its output dimension and size formulas, are systematically shown in Formulas (14), (15), and (16), providing a comprehensive mathematical description.

$$X \in \mathbb{R}^{C_{in}\times D_{in}\times H_{in}\times W_{in}} \tag{12}$$

$$K \in \mathbb{R}^{K_D\times K_H\times K_W\times C_{in}\times C_{out}} \tag{13}$$

$$Y_{c,d,h,w} = \sum_{k_d=0}^{K_D-1}\sum_{k_h=0}^{K_H-1}\sum_{k_w=0}^{K_W-1}\sum_{c_{in}=0}^{C_{in}-1} X_{c_{in},d+k_d,h+k_h,w+k_w}\cdot K_{k_d,k_h,k_w,c_{in},c} + b_c \tag{14}$$

$$Y \in \mathbb{R}^{C_{out}\times D_{out}\times H_{out}\times W_{out}} \tag{15}$$

$$D_{out} = H_{out} = W_{out} = \left[\frac{D_{in} + 2\times padding - K_D}{stride}\right] + 1 \tag{16}$$

In the AI-CFD model, the input channel dimension is set as C_{in}=4, with spatial dimensions $D_{in} = H_{in} = W_{in}$ = 100. The 3D convolution kernel dimensions are $K_D = K_H = K_W$ = 3, and the output channel dimension C_{out} is a learnable parameter. The value $Y_{c,d,h,w}$ denotes the element of the overall output tensor at channel c and spatial location (d,h,w). In practical experiments, the size of the local output tensor also depends on the batchsize. The term $K_{k_d,k_h,k_w,c_{in},c}$ represents the weight of the convolution kernel at spatial position $(k_d,k_h,k_w$), input channelc_{in}, and output channel c, while b_c denotes the bias term for output channel c.

After completing the 3D convolution operation, the model proceeds to 1D convolution processing. Unlike the joint operation of 3D convolution in spatial and channel dimensions, 1D convolution independently performs feature transformation at each spatial position (d,h,w). Specifically, all channel values at positions (d,h,w) in the output tensor are only obtained by weighting and summing the channel dimension vectors at the corresponding positions in the input tensor using convolution kernels. The convolution kernel parameters are not shared in the spatial dimension and do not undergo sliding operations. This computational property allows 1D convolution to be viewed as performing independent linear transformations on the channel vectors at each spatial position, thereby fully parallelizing the computation of all spatial positions. At this point, the convolution kernel tensor parameters and output tensor calculation method of 1D convolution are shown in formulas (17) and (18), the input channel dimension is set as C_{in}=4：

$$K \in \mathbb{R}^{1\times1\times1\times C_{in}\times C_{out}} \tag{17}$$

$$Y_{c,d,h,w} = \sum_{C_{in}=0}^{C_{in}-1} X_{C_{in},d,h,w} \cdot K_{0,0,0,c_{in},c} + b_c \tag{18}$$

Following the output of the Spatial convolution layer, the data is processed through a specially designed Channels Merge convolution layer with the tensor dimension of $C_{low} \times 100 \times 100 \times 100$ and its main function is to accurately adjust the feature dimension, providing adaptive support for subsequent skip connection operations. This design effectively enhances the stability of the model in deep network training and significantly improves its feature expression ability.

The multi CNN architecture composed of Spatial convolutional layer and Channels Merge convolutional layer assumes the feature embedding function of Transformer network in this model. This design is a unique innovation proposed in this article for the SOEC three-dimensional physical field distribution prediction task, which is significantly different from the traditional Transformer network architecture.

3. Experiment and Discussion of AI-CFD Prediction Model for SOEC 3D Temperature and Current Density Fields

3.1 Related Hyperparameters Settings Before Experiment

This chapter will evaluate the performance of the improved Transformer AI CFD model through experiments, mainly including predicting and reconstructing the distribution of the internal temperature field and current density field of SOEC. Before conducting the experiments, the relevant hyperparameters of the constructed improved Transformer-AI-CFD model were first set, including:

1.The number of Spatial convolutional layers was set to N=2, with the convolution kernel using padding=1 and stride=1;

2.The number of layers in both the Transformer encoder and decoder structures was set to N=2, the overall network learning rate was set to 0.01, the number of attention heads was 4, and the number of hidden layers was 64.

All experimental data were derived from Ansys Fluent simulation data, and all experiments were conducted on the following hardware specifications:RAM (Random Access Memory): 48 GB; CPU(Central Processing Unit): Intel(R) Core(TM) i7-10700 CPU@2.90GHz; GPU(Graphical Processing Unit): NVIDIA RTX 4060 (8GB); Storage: 2.05 TB; System Version: Windows 10.

3.2 Criterion Under Different Test Conditions

To evaluate the Transformer model's prediction accuracy, this study employs two quantitative metrics:Root Mean Squared Error (MSE) and Mean Absolute Error (MAE), defined in Formulas (19) and (20), respectively.

$$RMSE = \sqrt{\frac{1}{n}\sum_{i=1}^{n}(y_i - \hat{y}_i)^2} \tag{19}$$

$$MAE = \frac{1}{n}\sum_{i=1}^{n}|y_i - \hat{y}_i| \tag{20}$$

Among it, n denotes the sample size, and $y_i - \hat{y}_i$ represents the deviation between the true value and predicted value of sample i. MSE quantifies the square root of the average squared error, where larger deviations are quadratically amplified—making it sensitive to outliers. This characteristic makes RMSE particularly suitable for evaluating energy-related errors in SOEC, where rare but severe thermal anomalies must be detected.

In contrast to RMSE, MAE calculates the average absolute deviation, reducing the influence of outliers. This metric provides an intuitive measure of typical prediction errors,

ideal for quantifying temperature discrepancies in practical applications. For instance, a MAE of 2 K in SOEC temperature fields indicates that predicted values typically deviate by 2 K from true values, a critical threshold for operational safety.

The choice of these metrics balances precision and robustness: RMSE emphasizes overall prediction fidelity, while MAE ensures reliability in routine operations. As shown in subsequent experiments, the model achieves an RMSE and an MAE both within 2 K in the reconstruction of temperature field spatial contours of SOEC, demonstrating its suitability for both rigorous error analysis and practical field monitoring.

3.3 Experiment Steps

During the experimental phase, the research team inputted dozens of sets of SOEC CFD simulation data under different boundary conditions into the neural network. Given that a single set of simulation data contains millions of three-dimensional grid points, in order to balance computational efficiency and model generalization ability, the research team adopted a three-dimensional spatial block partitioning strategy. Specifically, the overall three-dimensional computational domain of each set of simulation data is discretized into hundreds of spatially adjacent and non overlapping sub blocks, with each sub block retaining the complete physical parameter tensor structure. Subsequently, a random sampling method was used to independently extract the training set and validation set from all blocks, ensuring that each operating condition has statistical representativeness in the dataset distribution.

During the model training process, the research team used a learning rate optimization strategy system to explore the impact of hyperparameters on model convergence. Four sets of

comparative experiments were specifically set up, with learning rates of 0.05, 0.01, 0.005, and 0.001, respectively, while the remaining training parameters remained strictly consistent. The optimization process adopts the Adam adaptive optimization algorithm, with a batch size set to 16 and a training round limit of 300. At the same time, the early stop mechanism is enabled to avoid overfitting after 20 epochs without validation loss improvement. The loss function uses mean square error (MSE) as the evaluation metric. The loss curves of the training set and validation set are shown in Figures 6 and 7, and the trend of the curves reflects the significant impact of different learning rates on the convergence speed and generalization performance of the model. After analyzing the dynamic characteristics of the loss function, for the sake of saving computing power, the optimal learning rate is ultimately determined as 0.05, laying the foundation for subsequent physical field prediction experiments.

In the process of reconstructing and predicting the physical field spatial contour map of SOEC, a diagonal hierarchical prediction path is followed from the inside out, starting from the spatial geometric center and expanding outward layer by layer along the diagonal direction of the octahedral structure (such as the $\pm x \pm y \pm z$ combination direction). Specifically, each predicted path corresponds to an octahedral surface defined by "equal sum of absolute coordinate values" (such as the k-th layer satisfying $|x| + |y| + |z| = k$). Starting from the core region (vertices (1,0,0), (0,1,0), etc. when k=1), the predicted path sequentially traverses the grid points in each diagonal direction according to the hexagram limit. After completing each layer, it expands outward at equal steps to the next layer (such as $k \rightarrow k$+1), forming a spiral prediction trajectory similar to "octahedral nesting". This path extends symmetrically and

uniformly through layers, ensuring that the physical field spatial contour map is gradually reconstructed from the core area to the boundary area in three-dimensional space, covering both the main direction of the xyz coordinate axis and the feature distribution in the diagonal direction, thereby improving the spatial consistency and detail integrity of the prediction results. Upon completion of the prediction process, the results are transmitted to a Unity3D-based SOEC visualization system. Leveraging point cloud technology, this system enables real-time rendering of physical field spatial contour maps, dynamically visualizing temperature, voltage, and other scalar distributions in three-dimensional space. The combination of the hierarchical prediction path and advanced visualization framework provides an intuitive and accurate representation of complex multiphysics field distributions within the SOEC, facilitating in-depth analysis of electrochemical reaction mechanisms and structural optimization.

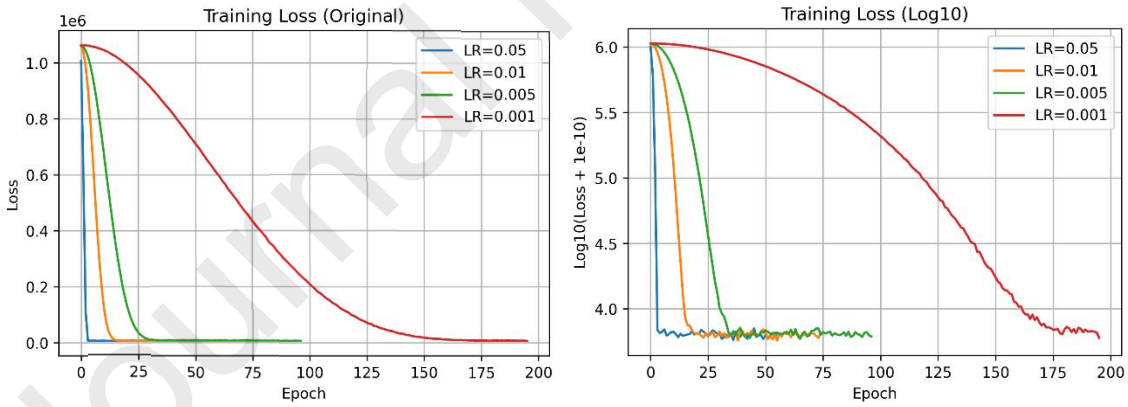

Fig.6 Training loss of AI-CFD model under different learning rates

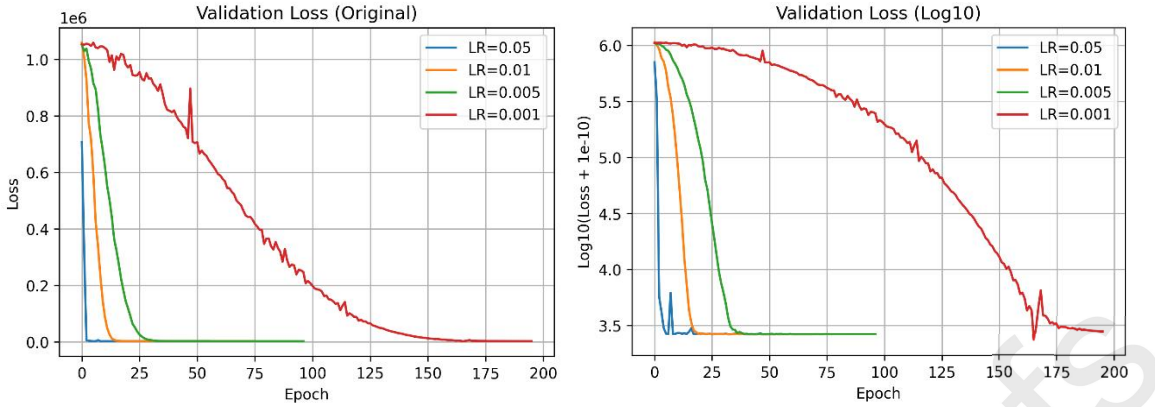

Fig.7 Validation loss of AI-CFD model under different learning rates

3.4 Experiment Results Under Different Conditions

To evaluate the generalization performance of the model in predicting temperature and current density distributions, this paper first employed k-fold cross validation (k=5) on the entire CFD dataset, which consists of 80 independent simulation cases covering both traditional and extreme boundary conditions. For temperature field prediction, the dataset is randomly divided into 5 mutually exclusive subsets. In each validation iteration, one subset is designated as the test set, while the remaining four subsets are combined together to form the training set. The training prediction process is repeated 5 times to ensure that each case is accurately included in the temperature field prediction test once.

The cross validation results of temperature field prediction show that the average mean absolute error (MAE) of 5 iterations is 1.05, and the root mean square error (RMSE) is 1.32. The iterative error fluctuations of MAE and RMSE are within ± 0.3 and ± 0.2, respectively. These results indicate that the model maintains stable prediction accuracy for temperature fields in different test subsets - all of which are independent CFD cases that do not participate in training - confirming that data overlap or concentrated boundary cases do not cause

performance distortion.

For the current density field prediction, the same k-fold cross validation framework (k=5) was applied to the CFD dataset of 80 cases to ensure consistency between data partitioning and validation logic and temperature field evaluation. The results showed that the average MAE of 5 iterations was 24.5, and the average RMSE was 26.8. The error fluctuations of MAE and RMSE are within ± 3.0 and ± 3.5, respectively. This stability indicates that the predictive performance of the model for current density fields is reliable on different test subsets.

In order to further visualize the model's ability to predict these two domains, three additional test cases (including two non generalized extreme operating conditions) were manually selected. The performance of the model under these conditions was evaluated using MAE and RMSE with temperature and current density fields, clearly demonstrating its behavior under special circumstances. The test conditions are shown in Table 1, temperature prediction spatial contour maps of Condition 1, Condition 2, and Condition 3 are shown in Figure 8 to 10 and current density prediction spatial contour maps of such conditions are shown in Figure 11 to 13, respectively.

Table.1 Testing conditions

Condition Number	Electrolysis Temperature/K	Electrolysis Voltage/V	Ratio of H_2O/H_2/%	Inlet Air Mass Flow/kg/s
Condition 1	1023	13	90	0.00065
Condition 2	973	12	70	0.00065
Condition 3	1073	14	80	0.00075

(1) Temperature prediction spatial contour maps

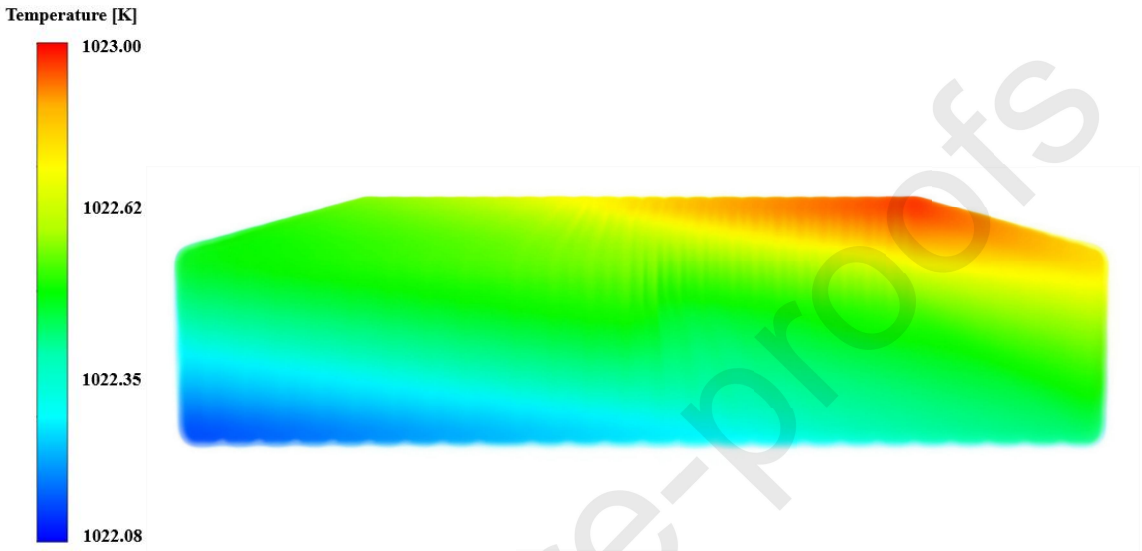

(a) SOEC 3D temperature prediction spatial contour map

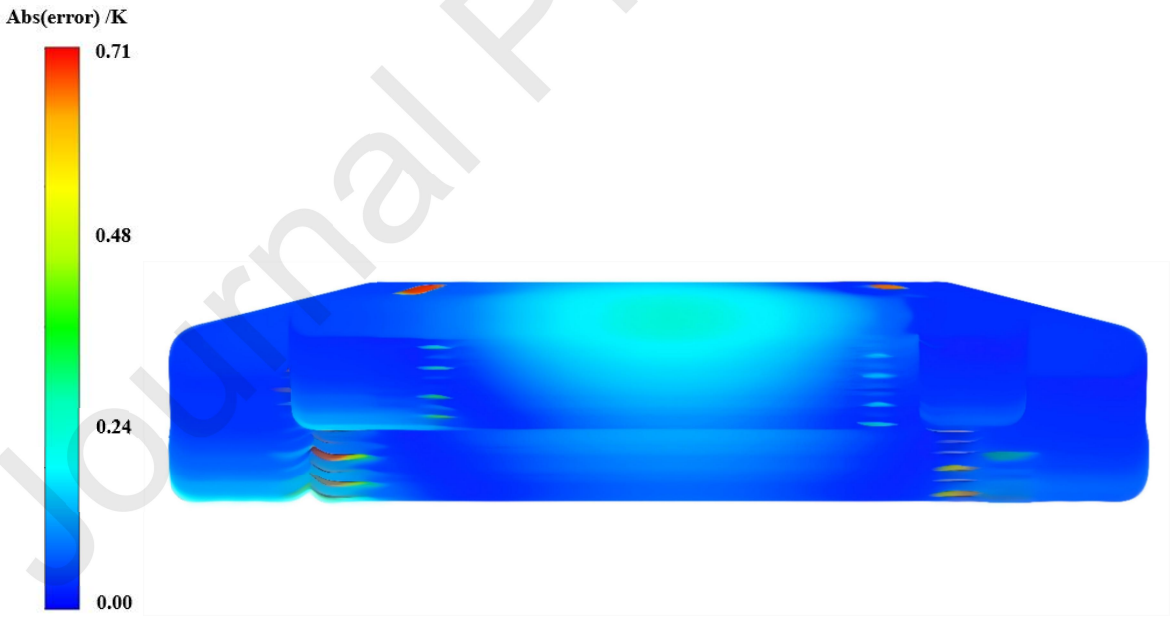

(b) SOEC 3D temperature prediction error spatial contour map

Fig.8 Diagrammatic sketch of temperature prediction for condition 1

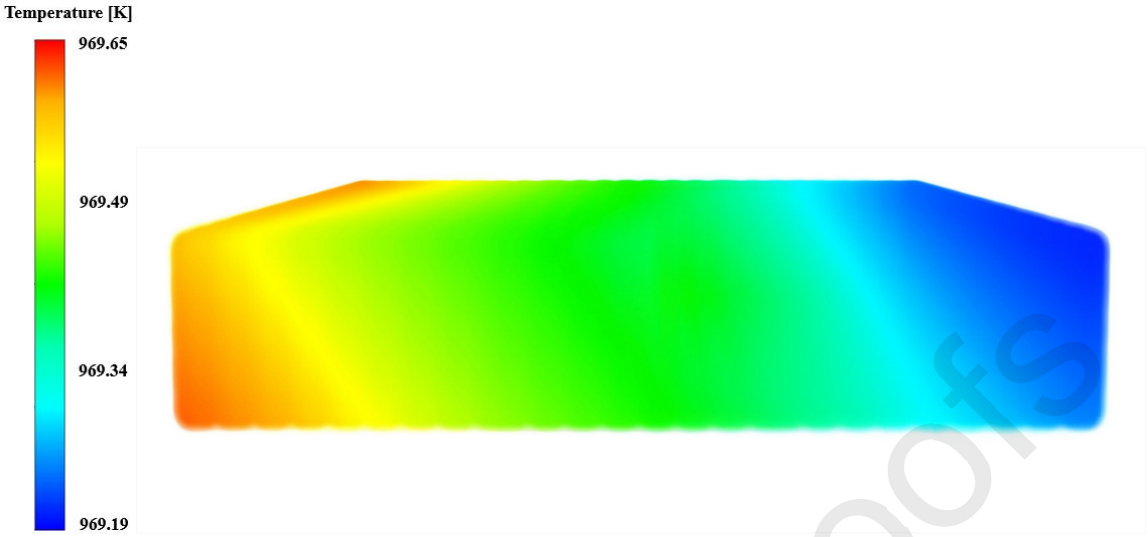

(a) SOEC 3D temperature prediction spatial contour map

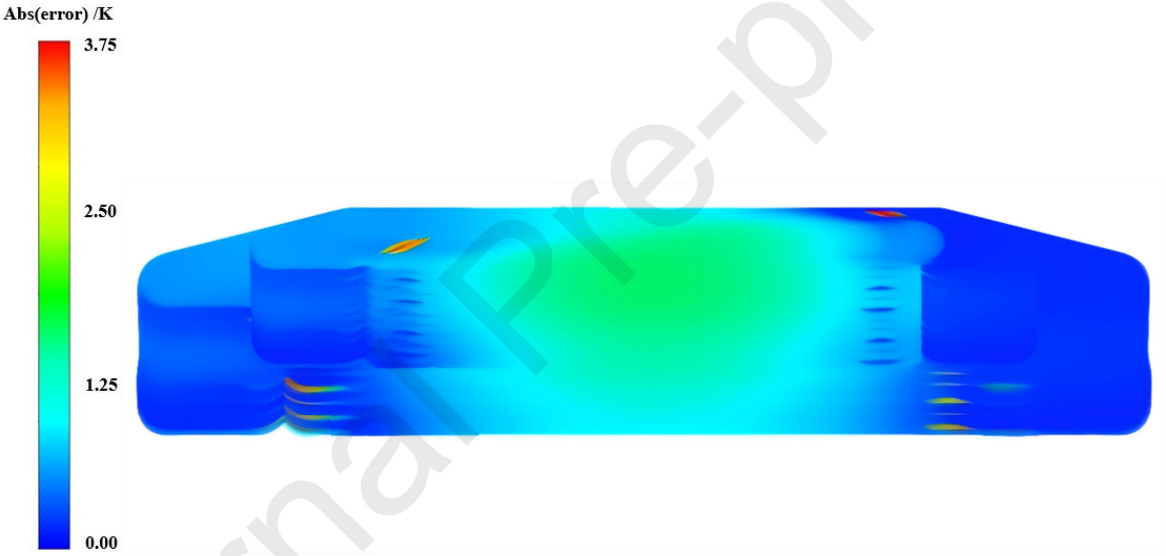

(b) SOEC 3D temperature prediction error spatial contour map

Fig.9 Diagrammatic sketch of temperature prediction for condition 2

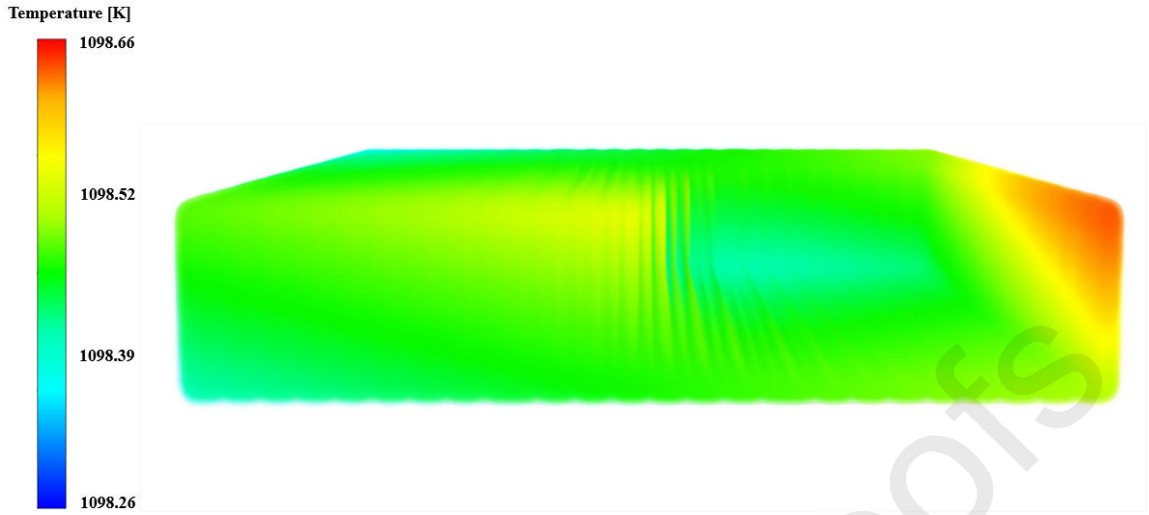

(a) SOEC 3D temperature prediction spatial contour map

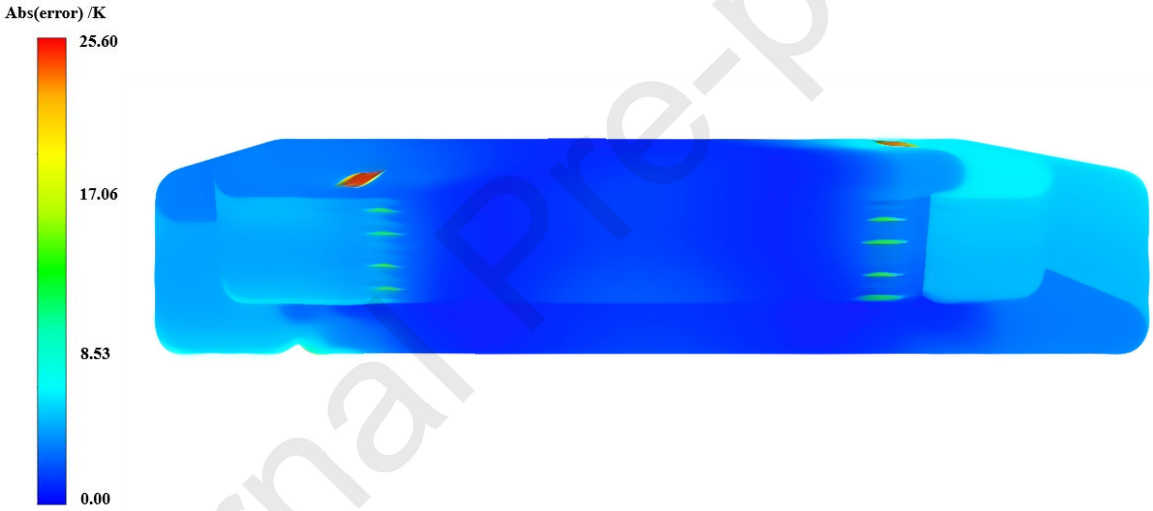

(b) SOEC 3D temperature prediction error spatial contour map

Fig.10 Diagrammatic sketch of temperature prediction for condition 3

As to condition 1, the RMSE of condition 1 is 0.41, the MAE is 0.24, and the absolute temperature error at the maximum point is 0.71 K. It is worth mentioning that condition 1 is a training condition in the training set, while conditions 2 and 3 are generalization conditions that are not in the training set. As to condition 2, the RMSE is 1.52, the MAE is 1.35, and the absolute temperature error at the maximum point is 3.75 K.As to condition 3, the RMSE is 1.77, the MAE is 1.68, and the absolute error at the maximum point is 25.60 K. The error spatial

contour map reveals that larger errors tend to concentrate in the inlet and outlet flow channels, whereas the temperature prediction of the SOEC's internal electrolyte layer exhibits higher accuracy. This discrepancy arises from the distinct heat transfer characteristics of the two regions: the internal electrolyte layer operates in a relatively stable thermal environment dominated by conduction—an inherently simpler heat transfer mechanism that allows for more precise predictions. In contrast, the inlet and outlet flow channels involve more complex heat transfer processes , which introduces greater challenges to accurate prediction and thus results in higher errors.

(1) Current density prediction spatial contour maps

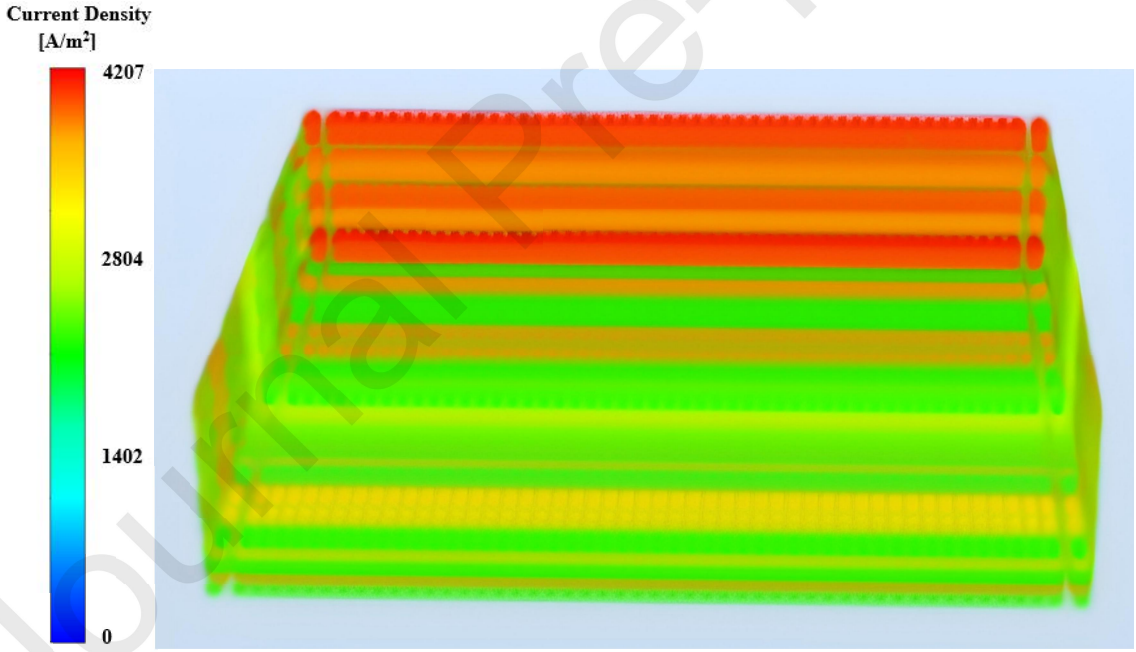

(a) SOEC 3D current density prediction spatial contour map

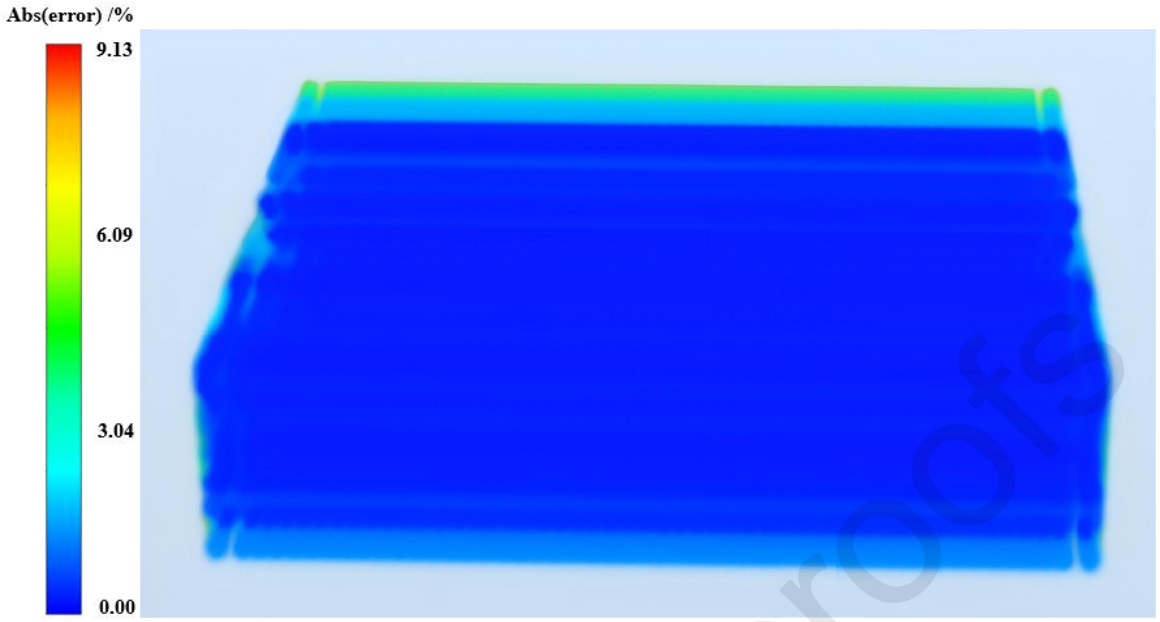

(b) SOEC 3D temperature prediction error spatial contour map

Fig.11 Diagrammatic sketch of current density prediction for condition 1

When the current density is predicted, due to the complex electrolyte layer structure in SOEC, the current density distribution fluctuates greatly, so the corresponding block division and adjustment must be carried out according to the internal geometry structure, and finally a good prediction result is achieved. For condition 1, the MAE is 25.31, the RMSE is 28.65 and the maximum error value of current density prediction is 9.13%.

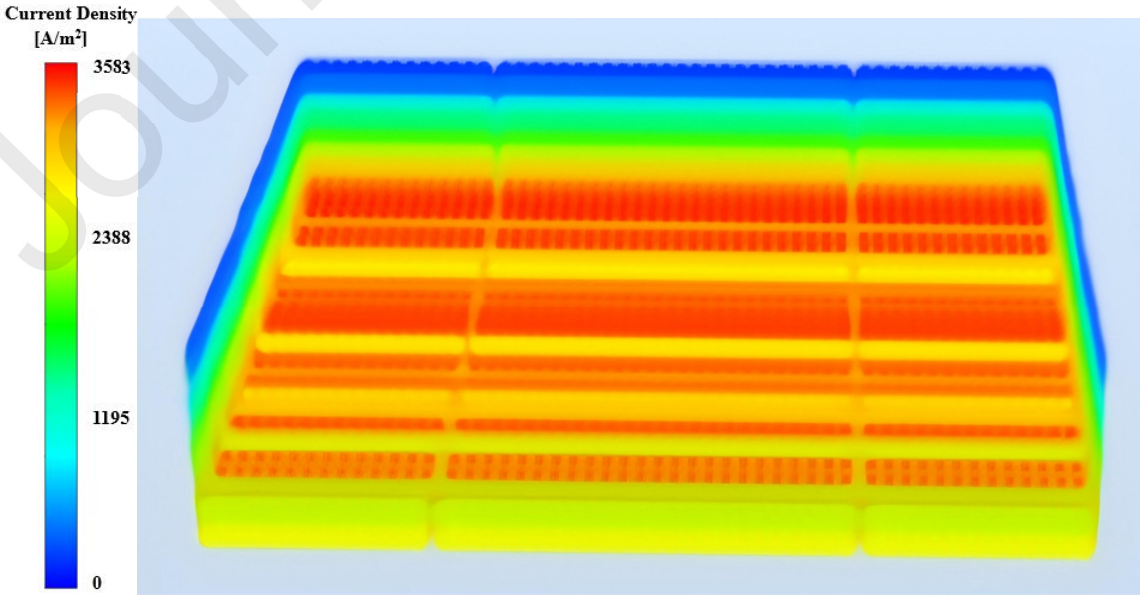

(a) SOEC 3D current density prediction spatial contour map

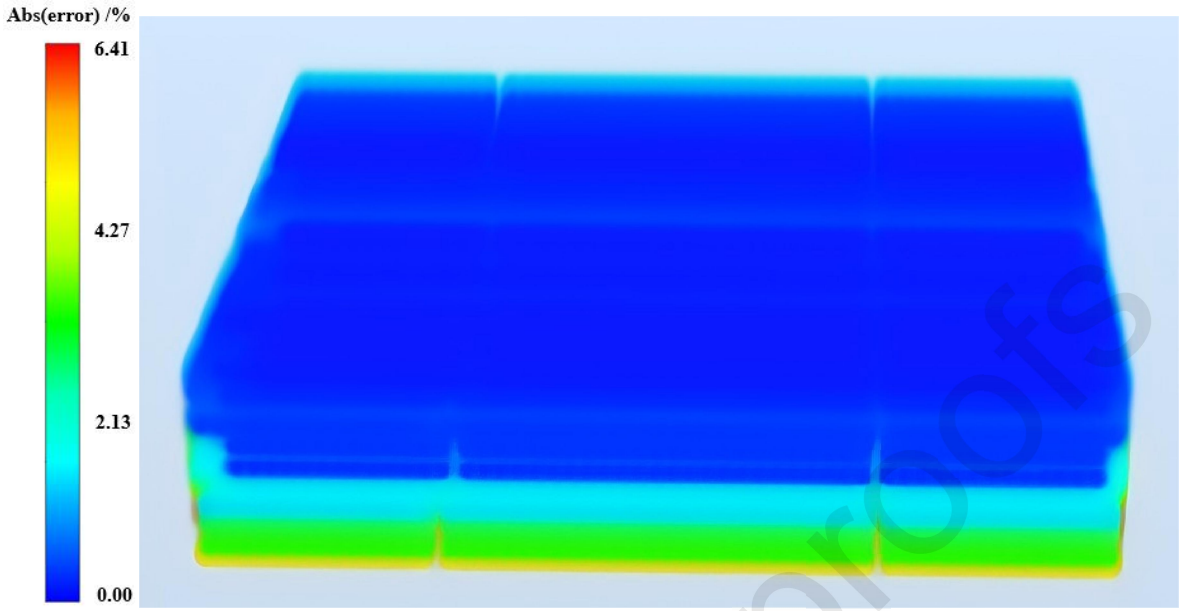

(b) SOEC 3D temperature prediction error spatial contour map

Fig.12 Diagrammatic sketch of current density prediction for condition 2

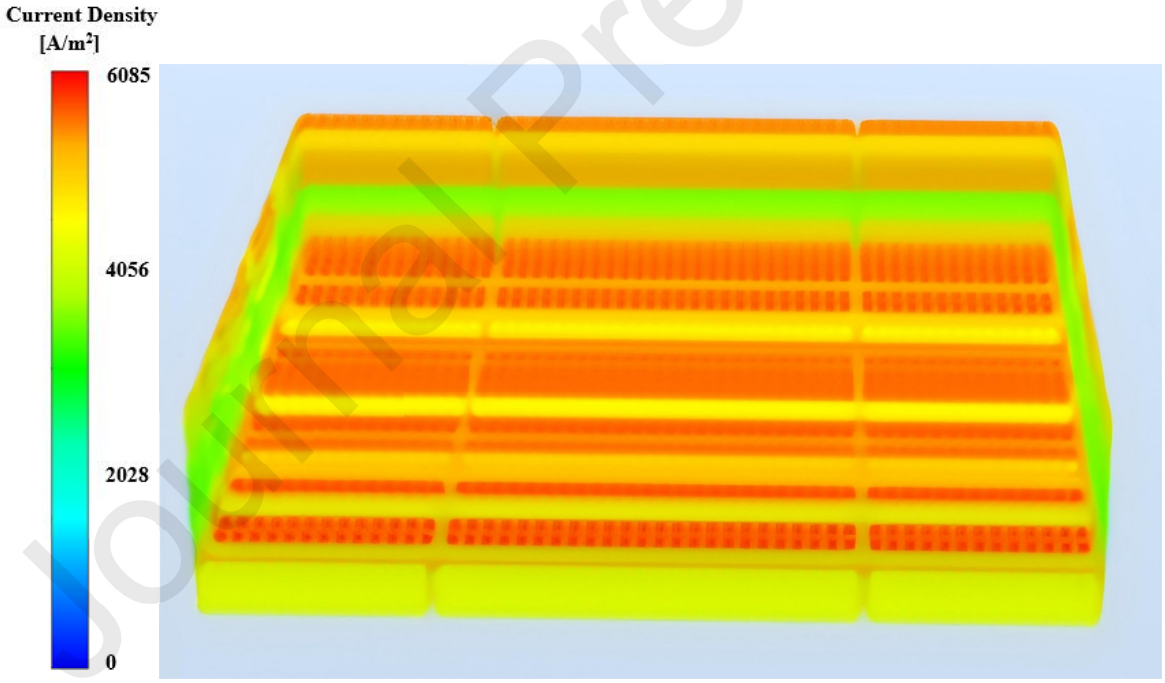

(a) SOEC 3D current density prediction spatial contour map

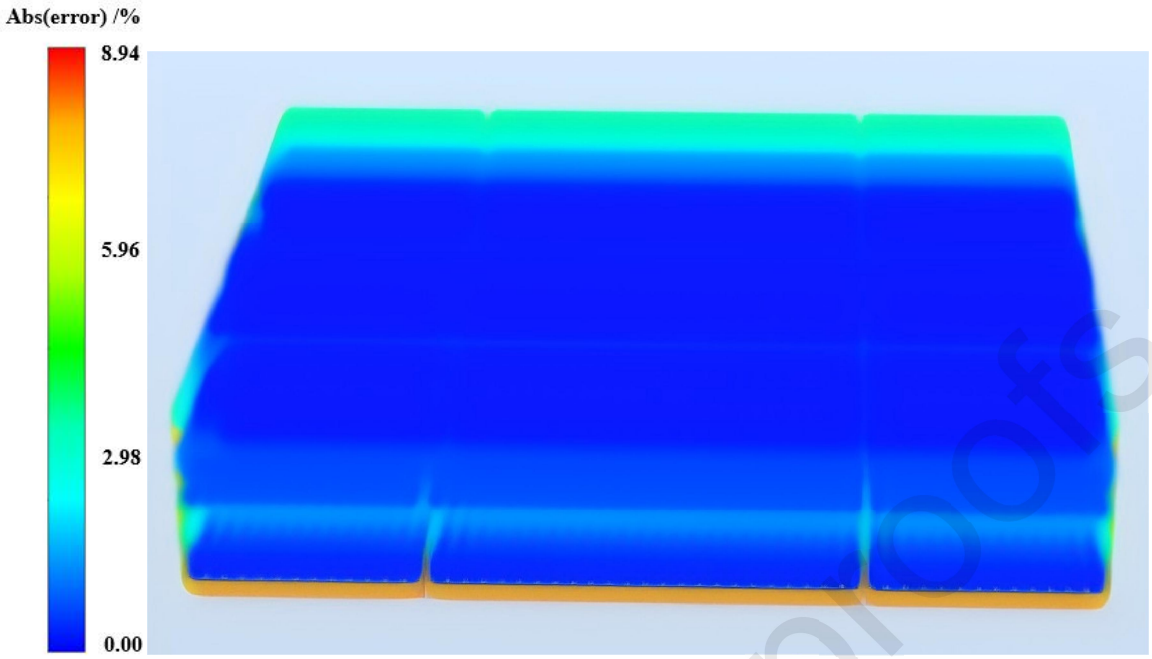

(b) SOEC 3D temperature prediction error spatial contour map

Fig.13 Diagrammatic sketch of current density prediction for condition 3

For condition 2, the MAE is 15.86, the RMSE is 18.23 and the maximum error is 6.41% while for condition 3, the MAE is 39.67, the RMSE is 42.19 and the maximum error is 8.94%, both of which have good prediction accuracy. The overall evaluation indicators for predicting the temperature field and current density field under three operating conditions are shown in Table 2:

Table.2 Overall evaluation indicators

Condition Number	MAE (Temperature)	RMSE (Temperature)	MAE (Current Density)	RMSE (Current Density)
Condition 1	0.24	0.41	25.31	28.65
Condition 2	1.35	1.52	15.86	18.23
Condition 3	1.68	1.77	39.67	42.19

Based on the analysis of the prediction results, it can be seen that due to the small temperature difference between the upper and lower limits of the internal temperature field of SOEC, the overall prediction error of the Transformer model is also small. However, the current density field inside the SOEC not only shows a significant difference between upper and lower limits but also large distribution fluctuations, resulting in relatively larger prediction errors. This is mainly because current density distribution is highly sensitive to various parameters—even minor changes in these parameters can cause it to fluctuate drastically, thereby amplifying simulation errors. Nevertheless, the overall prediction accuracy is still relatively good.

3.5 Discussion

3.5.1 Ablation Experiments

After verifying the accuracy of the modified Transformer AI-CFD model constructed in this paper, ablation experiments were further conducted to validate the effectiveness of the CNN-based feature extraction Spatial Convolution layer in the model architecture. Ablation experiments were performed with the number of layers set to 0, 1, 2, and 3, respectively. The predicted physical field was the current density distribution under Condition 1, and the aggregated results of evaluation metrics are shown in Figure 14. As shown in the figure, when the number of Spatial Convolution layers is 0 or 1, both the Root Mean Squared Error (RMSE) and Mean Absolute Error (MAE) are relatively large, indicating poor prediction performance of the model. In contrast, when the number of layers is 2 or 3, the prediction performance is significantly improved, which fully demonstrates the critical role of the Spatial Convolution layer in the modified Transformer model proposed in this study. The number of Spatial

Convolution layers was ultimately set to 2 for the following reasons: although both configurations with 2 and 3 layers exhibit good prediction performance, increasing the layer count to 3 introduces excessive convolutional layers. This not only consumes more computational resources but also raises the risk of overfitting. Moreover, the performance improvement achieved by 3 layers is marginal compared to that of 2 layers. Therefore, a configuration with 2 Spatial Convolution layers was selected as the optimal solution to balance model efficiency and prediction accuracy.

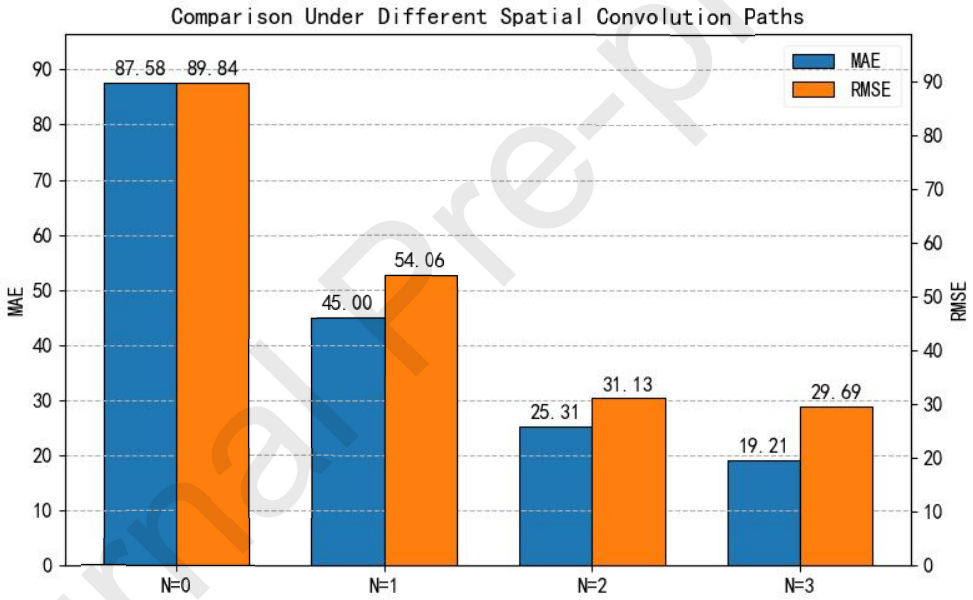

Fig.14 Ablation Experiments on Spatial Convolution

Subsequently, ablation experiments were conducted on the prediction paths of the model during three-dimensional physical field reconstruction. First, an axis-aligned hierarchical expansion path was used to systematically traverse the spatial grid points. The axis-aligned hierarchical expansion path starts from the spatial geometric center and extends outward layer by layer in a cubic nesting pattern. Each layer corresponds to the surface of an axis-aligned cube, with its coordinate extension ranges in the three coordinate axis directions exhibiting

symmetric distribution characteristics: in the x-axis direction, extending l times the unit step size Δx from the central coordinate cx to both sides; in the y-axis direction, extending l times the unit step size Δy from the central coordinate cy to both sides; in the z-axis direction, extending l times the unit step size Δz from the central coordinate cz to both sides. The traversal order follows a three-axis round-trip closed-loop pattern: forming a closed path along the positive → negative x-axis, positive → negative y-axis, and positive → negative z-axis directions. This path ensures that all grid points on the surface of each layer's cube are fully visited, with the maximum absolute coordinate value increasing linearly with the number of layers ($\max(|x|,|y|,|z|)=l \cdot \Delta$). Through layer-by-layer expansion (l=0,1,2,…), the path gradually covers the entire space from a single central point. This strategy separates the traversal order of the coordinate axes, reduces the complexity of three-dimensional sampling, and ensures isotropic feature coverage.

Next, a diagonal hierarchical expansion path (octahedral structure) was adopted, with the spatial origin as the center, and layer-by-layer expansion was performed based on the octahedral surface equation $|x| + |y| + |z| = k$, where k is the number of layers (k=0,1,2,…). The core mechanism of this path is to achieve systematic coverage of the diagonal directions in three-dimensional space through equidistant increments of the sum of coordinate absolute values. Specifically, the k-th layer includes all grid points satisfying $|x| + |y| + |z| = k$, forming an octahedral surface centered at the origin. The inner layer (k=1) corresponds to the vertices of the octahedron, such as (1,0,0), (0,1,0), etc.; as k increases, the outer layers gradually include more points in diagonal directions (such as (2,0,0), (1,1,0) when k=2), forming an "octahedral

nesting" structure. The traversal order follows the principle of octant priority, sequentially visiting the eight octants of the octahedron, with vertices and edges traversed in diagonal directions within each layer. The mathematical logic of this path ensures spatial symmetry and balanced sampling of diagonal features, making it suitable for capturing anisotropic distributions in physical fields (such as multi-directional diffusion processes in SOEC). Through layer-by-layer expansion, the path gradually covers the entire space from the core vertices, and the linear growth characteristic of the sum of coordinate absolute values ($k \rightarrow k+1$) ensures the hierarchical and complete feature extraction.

Finally, a spiral hierarchical expansion path was adopted, with the spatial origin as the center, achieving spiral layer-by-layer expansion through polar or spherical coordinate systems. In the cylindrical coordinate system, the path forms multiple cylindrical shells along the increasing radius r. Each layer has a fixed radius r_k, with the angle θ continuously varying from 0 to 2π, and the z-coordinate can remain fixed (planar spiral) or rise synchronously in a spiral (3D spiral). In the spherical coordinate system, the path forms spherical shells with increasing radius r, and each layer traverses the polar angle $\theta \in [0,\pi]$ and azimuthal angle $\phi \in [0,\pi]$ to achieve full coverage of the spherical shell surface. The core mechanism of this path is to form a spiral trajectory through the equidistant expansion of the radius $r(r_1 \rightarrow r_2 \rightarrow \ldots)$ and continuous angular sampling. For example, starting from the initial point $(r_1,0,0)$, after completing the θ-traversal along the circumference, the radius increases to r_2, and the traversal is repeated, forming a "spiral nesting" structure. This strategy effectively reduces the complexity of 3D spatial sampling by separating the traversal order of radial and angular

directions, making it suitable for predicting physical fields with cylindrical or spherical symmetry (such as temperature distribution in pipe flows or concentration fields in spherical reactors). The continuity and isotropic characteristics of spiral expansion ensure that the model uniformly captures spatial details, enhancing the spatial smoothness and physical rationality of prediction results. The overall results are shown in Figure 15 and therefore, the diagonal hierarchical expansion path is chosen as the optimal solution to achieve the best prediction accuracy.

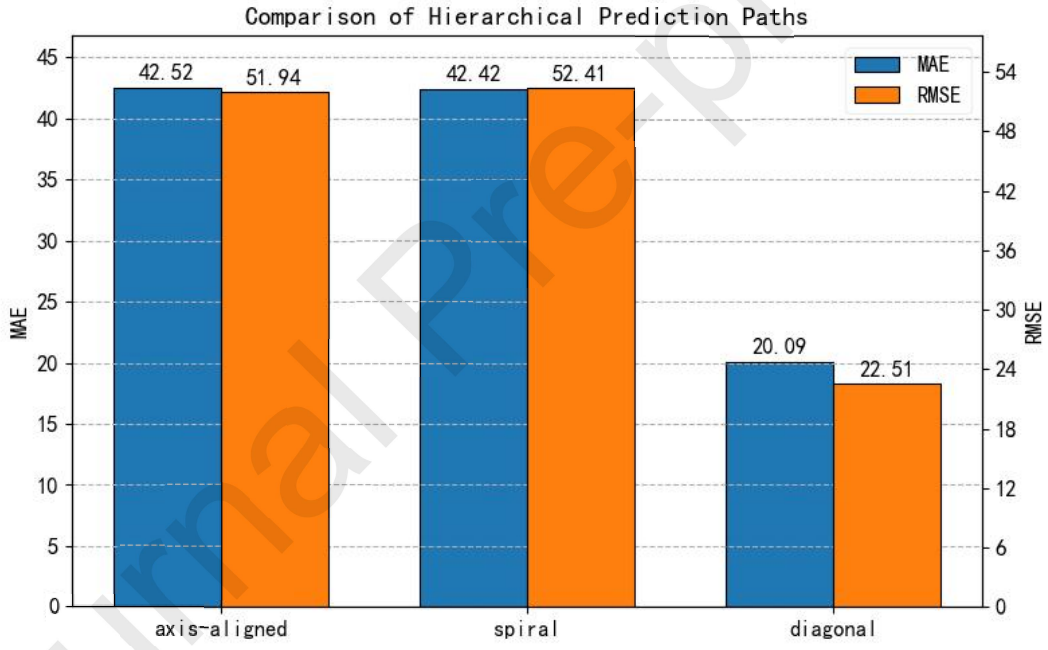

Fig.15 Ablation Experiments on Hierarchical Prediction Paths

3.5.2 Comparative Experiments

After conducting ablation experiments on the Spatial Convolution layer, this paper also conducted three precision comparison experiments between the constructed modified Transformer AI-CFD model and the traditional Gaussian interpolation prediction method, with the aim of reconstructing the temperature field; At the same time, three hardware utilization

comparison experiments were conducted with traditional CFD simulation methods, and the results are shown in Tables 3 and 4:

Table.3 Comparison Results of Accuracy Experiment

Criterion	Application method					
	Modified Transformer			Gaussian interpolation		
RMSE	Average	Minimum	Maximum	Average	Minimum	Maximum
	1.37	0.41	1.77	72.9	65.2	82.6
MAE	Average	Minimum	Maximum	Average	Minimum	Maximum
	1.09	0.24	1.68	66.53	60.84	73.12

Table.4 Comparison Results of Hardware Utilization Experiment

Criterion	Application method					
	Modified Transformer			CFD Simulation		
	Average	Minimum	Maximum	Average	Minimum	Maximum
Time	3min28s	2min05s	4min39s	3h55min	3h42min	4h28min
CPU	11%	11%	12%	15%	14%	17%
GPU	1%	0	1%	0	0	1%

RAM	32%	31%	32%	56%	55%	56%

From above, it can be seen that the modified Transformer AI-CFD model developed in this study demonstrates superior accuracy compared to traditional interpolation algorithms and significantly enhanced timeliness relative to conventional CFD simulation algorithms. This model not only reduces computational resource consumption substantially but also exhibits strong application potential in scenarios requiring efficient and precise physical field prediction.

4. Conclusion

In summary, this article constructed a neural network model based on Transformer, which can reconstruct the temperature and current density fields and predict the spatial contour map for the three-dimensional temperature and current density distribution inside SOEC. The global max error rate is controlled below 9% and the global average error is controlled below 5%. And the prediction time is controlled at the level of minutes and seconds, effectively solving the problem of time-consuming of CFD simulation methods in the past. By combining CFD simulation with neural network intelligent models, intelligent operation and maintenance monitoring of SOEC can be successfully achieved. In the future, further training of neural network models can be conducted on the distribution of other physical fields such as water vapor content to achieve multi-objective optimization.

Acknowledgements

This work was supported by key project of National Natural Science Foundation of China

under Grant No. 22393954.

Declaration of competing interest

The authors declare that they have no known competing financial interests or personal relationships that could have appeared to influence the work reported in this paper.

Data availability

The data that support the findings of this study are available from Sinopec. Restrictions apply to the availability of these data, which were used under license for this study. Data are available from Dr. Jun Cao with the permission of Sinopec.

References

[1] J. Aicart, F. Usseglio-Viretta, J. Laurencin, , et al ,Operating maps of high temperature H2O electrolysis and H2O+CO2 co-electrolysis in solid oxide cells,International Journal of Hydrogen Energy,Volume 41, Issue 39,2016,Pages 17233-17246,ISSN 0360-3199, https://doi.org/10.1016/j.ijhydene.2016.07.269.

[2] Shuang Zong, Xiufei Zhao, Linda L. Jewell, et al. Advances and challenges with SOEC high temperature co-electrolysis of CO2/H2O: Materials development and technological design,Carbon Capture Science & Technology,Volume 12,2024,100234,ISSN 2772-6568, https://doi.org/10.1016/j.ccst.2024.100234.

[3] Mohamed J. Saadh, Diana Katherine Campoverde Santos, et al. Energy, exergy, exergoeconomic, and exergoenvironmental analysis of an integrated hydrogen production and liquefaction process using the Allam-Z cycle, SOEC, and cryogenic refrigeration,International Journal of Hydrogen Energy,Volume 100,2025,Pages 1246-1265,ISSN 0360-3199, https://doi.org/10.1016/j.ijhydene.2024.12.293.

[4] Zainal B S, Ker P J, Mohamed H, et al. Recent advancement and assessment of green hydrogen production technologies[J]. Renewable and Sustainable Energy Reviews, 2024,

189: 113-128, https://doi.org/10.1016/j.rser.2023.113941.

[5] T. Nejat Veziroglu, Conversion to Hydrogen Economy, Energy Procedia, Volume 29,2012,Pages 654-656,ISSN 1876-6102,https://doi.org/10.1016/j.egypro.2012.09.075.

[6] J. Aicart, F. Usseglio-Viretta, J. Laurencin,et al. Operating maps of high temperature H2O electrolysis and H2O+CO2 co-electrolysis in solid oxide cells,International Journal of HydrogenEnergy,Volume41,Issue39,2016,Pages17233-17246,3199,https://doi.org/10.1016/j.ijhydene.2016.07.269.

[7] Riezqa Andika, Asep Bayu Dani Nandiyanto, Zulfan Adi Putra, et al ,Co-electrolysis for power-to-methanol applications,Renewable and Sustainable Energy Reviews,Volume 95,2018,Pages 227-241,ISSN 1364-0321,https://doi.org/10.1016/j.rser.2018.07.030.

[8] Liuzhen Bian, Chuancheng Duan, Lijun Wang,et al， An all-oxide electrolysis cells for syngas production with tunable H2/CO yield via co-electrolysis of H2O and CO2,Journal of Power Sources,Volume 482,2021,228887, ISSN 0378-7753, https://doi.org/10.1016/j.jpowsour.2020.228887.

[9] Domenico Monopoli, Concetta Semeraro, Mohammad Ali Abdelkareem, Abdul Hai Alami, Abdul Ghani Olabi, Michele Dassisti, How to build a Digital Twin for operating PEM-Electrolyser system – A reference approach, Annual Reviews in Control, Volume 57,2024,100943,ISSN 1367-5788, https://doi.org/10.1016/j.arcontrol.2024.100943.

[10] Yitong Zheng, Zengbin Yin,Cutting temperature field online reconstruction using temporal convolution and deep learning networks,International Journal of Heat and Mass Transfer,Volume 241,2025,126766,ISSN 0017-9310,https://doi.org/10.1016 /j.ijheatmass transfer. 2025.126766.

[11] Yuluo Chen, Qiang Chen, Han Ma, Shuailong Chen, Qingguo Fei,Transfer machine learning framework for efficient full-field temperature response reconstruction of thermal protection structures with limited measurement data,International Journal of Heat and Mass Transfer,Volume 242,2025,126785,ISSN 0017-9310,https://doi.org/10.1016/ j.ijheatmasstransfer.2025.126785.

[12] Zeqi Hu, Yitong Wang, Hongwei Qi, Yongshuo She, Zunpeng Lin, Zhili Hu, Lin Hua,

Min Wu, Xunpeng Qin,Real-time 3D temperature field reconstruction for aluminum alloy forging die using Swin Transformer integrated deep learning framework,Applied Thermal Engineering,Volume 260,2025,125033,ISSN 1359-4311,https://doi.org/10.1016/j.applthermaleng.2024.125033.

[13] ZHANG M R; Wang E H; Mao J W,et al.Performance analysis of a metal-supported intermediate-temperature solid oxide electrolysis cell[J]. Frontiers in Energy Research. Volume 10 , Issue . 2022, https://doi.org/10.3389/fenrg.2022.888787.

Highlights

- Proposes an improved CNN-Transformer hybrid model for real-time prediction of SOEC internal temperature field spatial contours, addressing the timeliness bottleneck of conventional CFD simulations.
- Achieves temperature field reconstruction in seconds, reducing computational resource consumption by over 90% compared to traditional CFD simulations and ensures high prediction accuracy: temperature field MAE < 2 K, overall current density field prediction accuracy > 95%.
- Breaks through the timeliness bottleneck of conventional simulations, enabling technical support for intelligent operation and maintenance of SOEC digital twins, demonstrating significant engineering value for enhancing operational stability and intelligent management of SOEC systems.

Declaration of interests

☒ The authors declare that they have no known competing financial interests or personal relationships that could have appeared to influence the work reported in this paper.

☐ The authors declare the following financial interests/personal relationships which may be considered as potential competing interests: